ChemPubSoc Europe
DOI: 10.1002/celc.201901224
CHEMELECTROCHEM
Articles

The Key Role of Water Activity for the Operating Behavior and Dynamics of Oxygen Depolarized Cathodes

Maximilian Röhe,[a] Alexander Botz,[b] David Franzen,[c] Fabian Kubannek,[a] Barbara Ellendorff,[c] Denis Öhl,[b] Wolfgang Schuhmann,[b] Thomas Turek,[c] and Ulrike Krewer*[a]

Advanced chlor-alkali electrolysis with oxygen depolarized cathodes (ODC) requires 30% less electrical energy than conventional hydrogen-evolution-based technology. Herein, we confirm that the activities of hydroxide and water govern the ODC performance and its dynamics. Experimental characterization of ODC under varying mass transfer conditions on the liquid side reveals large differences in the polarization curves as well as in potential step responses of the electrodes. Under convective transport in the liquid electrolyte, the ODC is not limited by mass transfer in its current density at $j > 3.9\ \mathrm{kA\,m^{-2}}$, whereas transport limitations are already reached at $j \approx 1.3\ \mathrm{kA\,m^{-2}}$ with a stagnant electrolyte. Since gas phase conditions do not differ significantly between the measurements, these results are in contrast the common assumption that oxygen supply determines ODC performance. A dynamic model reveals the strong influence of the electrolyte mass transfer conditions on oxygen availability and thus performance. Dynamic responses of the current density to step-wise potential changes are dominated by the mass transport of water and hydroxide ions, which is by orders of magnitude faster with convective electrolyte flow. Without convective liquid electrolyte transport, a high accumulation of hydroxide ions significantly lowers the oxygen solubility. Thus, a fast mass transport of water and hydroxide is essential for high ODC performance and needs to be ensured for technical applications. The predicted accumulation of ions is furthermore validated experimentally by means of scanning electrochemical microscopy. We also show how the outlined processes can explain the distinctively different potential step responses with and without electrolyte convection.

1. Introduction

The oxygen reduction reaction (ORR) as given in eq. (1) in alkaline media is an essential process for many technical electrochemical applications, ranging from metal-air batteries or alkaline fuel cells to industrial-scale chlor-alkali electrolyzers.[1]

$$O_2 + 2\ H_2O + 4\ e^- \rightarrow 4\ OH^- \qquad (1)$$

For chlor-alkali electrolyzers, a high catalytic activity as well as a large interface between liquid electrolyte and gaseous oxygen are necessary to attain typical industrially required current densities of 4 to 6 $\mathrm{kA\,m^{-2}}$.[2] At the industrial operating conditions with NaOH concentrations exceeding 10 M and temperatures in the range of 80 to 90 °C,[3] silver offers a similar catalytic activity towards the ORR as compared to state-of-the-art catalysts such as platinum.[4] Therefore porous gas diffusion electrodes (GDE), so called oxygen depolarized cathodes (ODC), consisting of silver particles and polytetrafluoroethylene (PTFE) are utilized for industrial applications. The influence of variations in PTFE and the silver loadings are discussed in.[5] In our previous model-based study we explored the limiting processes of ODC.[6] We discovered that the consumption of water and the production of hydroxide ions induced by the electrochemical ORR lead to an enrichment of hydroxide ions at the gas-liquid interface within the liquid electrolyte. This causes a reduction in the availability of water, a change of the gas-liquid equilibrium and in consequence a substantial decrease of oxygen solubility. Based on these results we hypothesized that a fast mass transport of water and hydroxide ions across the porous electrode and the electrolyte diffusion layer outside the electrode are key drivers for a high ODC performance. Those findings are supported by experiments of Clausmeyer et al. who achieved higher current densities in a 5 M compared to a 10 M NaOH electrolyte utilizing single nanoparticle studies,[7] and by Botz et al. who measured an accumulation of hydroxide ions in the diffusion layer in close proximity to the ODC surface at higher current densities.[8] Furthermore, Zhang et al. presented a decreasing oxygen diffusivity in line with an increasing NaOH concentration and a decreasing water activity as a further limiting effect in ODC.[9]

The aforementioned studies demonstrate that the electrolyte has a significant influence on the ODC performance. Under careful consideration of the non-ideal behavior of water as a

---

[a] *M. Röhe, F. Kubannek, U. Krewer*
Institute of Energy and Process Systems Engineering, Technische Universität Braunschweig, Franz-Liszt-Str. 35, 38106 Braunschweig, Germany
E-mail: u.krewer@tu-braunschweig.de
[b] *A. Botz, D. Öhl, W. Schuhmann*
Analytical Chemistry – Center for Electrochemical Sciences, Faculty of Chemistry and Biochemistry, Ruhr University Bochum, Universitätsstr. 150, 44780 Bochum, Germany
[c] *D. Franzen, B. Ellendorff, T. Turek*
Institute of Chemical and Electrochemical Process Engineering, Technische Universität Clausthal, Leibnizstr. 17, 38678 Clausthal-Zellerfeld, Germany

solvent, the impact on the electrocatalytic properties of an ODC may be explained: In highly concentrated aqueous electrolytes, the activity of water, and its thermodynamics,[10] cannot be described by dilute solution theory. Instead, the activity coefficient strongly depends on the ion concentration.[11] The underlying mechanism of a decrease in water activity at increasing NaOH concentration is the formation of solvation shells, in which water molecules are bound to ions. In alkaline media, for instance, the first layer of the hydration shell of a hydroxide ion consists on average of four water molecules, whereas the coordination number decreases to about three at higher ion concentrations.[12] A decreased water activity goes, apart from the lower solubility of oxygen,[13] along with a change in mass transport,[14] a lower vapour pressure of the water[15] and slower reaction rate.[9] To completely elucidate the influence of the water activity on the ODC performance, a thorough analysis is required.

Dynamic simulations and measurements are a promising way to separate the processes affected by local water activity, to identify their interaction with the water activity and to unveil their influence on the electrode performance. This method has already been used successfully in many studies: Dynamic analysis was used for discriminating between reaction kinetic models e.g. for oxygen reduction[16] or methanol oxidation,[17] for quantifying the impact of reactant transport, e.g. of oxygen through liquid electrolyte on ORR performance,[18] for state estimation[19] or concentration sensing.[20]

In this work we confirmed the hypothesis that the water activity and its mass transport represents a crucial factor in governing the ODC performance. For this, stationary and dynamic measurements in two different electrochemical setups were conducted and analyzed with a one-dimensional dynamic three-phase model. Both set-ups had comparable conditions concerning the oxygen gas supply, yet they differed in the respective electrolyte conditions: The first experimental set-up was operated under convective electrolyte flow, whilst a stagnant electrolyte was present in the other one. Additionally, in the latter set-up, the analysis was assisted by scanning electrochemical microscopy (SECM), which allows for the determination of the hydroxide and water activities at a distance of about 1 μm above the ODC surface. We analyzed the differences in the dynamic behavior and steady state performance of both experimental cells using the dynamic model. By comparing the two cells, the influence of liquid phase mass transport and water activity in the liquid phase was assessed. We showed how both systems differ significantly in their performance and dynamics. The model-based analysis of dynamic measurements and the SECM measurements demonstrated that the performance and the dynamics of the ODC are highly dependent on the mass transport of water and hydroxide ions between the bulk phase and the electrode.

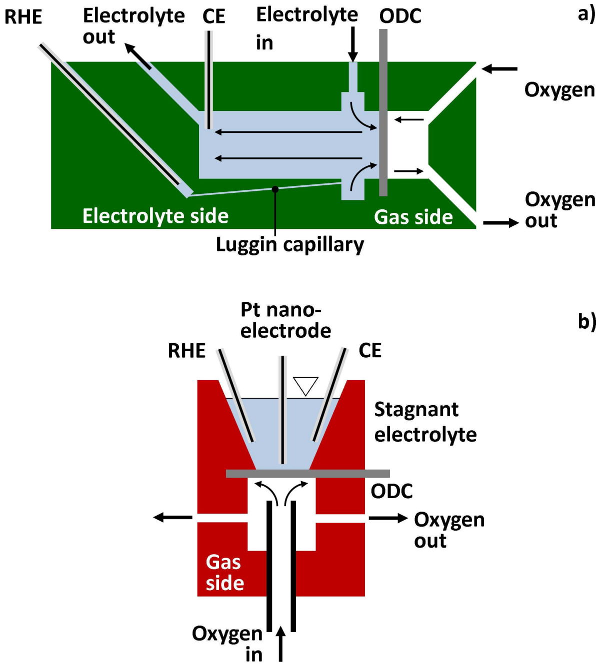

Figure 1. Schematic view of the used measuring cells with a) convective electrolyte flow, b) stagnant electrolyte.

Experimental

Two different electrochemical cells, as schematically depicted in Figure 1, were utilized and both were operated using identical ODC. As summarized in Table 1, the main factor differentiating both setups was the mass transport at the liquid side offered in the respective system. While the electrolyte was driven by a convective flow in the first set-up (con), it was stagnant in the second one (stag). In the first cell, the electrolyte temperature was controlled by regulating the temperature of the external electrolyte reservoir. In the second cell, an external heating circle had to be installed to enable temperature control without electrolyte flow. Furthermore, both set-ups differed in their geometrical cross section. Although both set-ups varied in the orientation of the ODC, no influence due to the hydrostatic pressure $p(h)$ is expected, as the height of electrolyte level h was approx. 1 cm for both set-ups, which leads to $p(h) \leq 150$ Pa. A detailed documentation of the set-up with the convective electrolyte flow is given in,[21] and for the cell with the stagnant electrolyte in.[8] In the latter set-up, SECM was used to

Table 1. Electrode characteristics

Name	Symbol	Unit	Convective electrolyte cell	Stagnant electrolyte cell
Electrode thickness	$z_{electrode}$	m	300×10^{-6}	295×10^{-6}
Geometrical cross section	A_{geo}	cm^2	3.14	0.264
Catalyst loading	θ_{Ag}	mg cm^{-2}	130.0	129.9
PTFE loading	θ_{PTFE}	mg cm^{-2}	4.0	4.1
Open circuit potential (measured)	E_0	V vs. RHE	1.095 V	1.10

quantify the hydroxide activity under stationary operating conditions.

ODC Preparation

The investigated ODC were fabricated by means of a wet spraying technique.[22] Silver particles (SF9ED Ag Flake, Ames Advanced Materials Corporation, $x_{50}=1.61$ µm), a methyl cellulose solution (1 wt-%, WALOCEL™ MKX 70000 PP 01) and additional demineralized water were mixed twice with an Ultra Turrax at 13500 rpm for five minutes until a homogeneous dispersion was obtained. Under a lower rotational speed of 1000 rpm, to prevent agglomeration, a PTFE dispersion (TF 5060GZ, 3 M™ Dyneon™) was added. Up to 90 layers of the suspension were applied on a nickel mesh as a conductive supporting material (106 µm × 118 µm mesh size, 63 µm thickness, Haver & Boecker) by using a spraying piston (Evolution, 0.6 mm pin hole, Harder & Steenbeck). The mechanical stability was improved in the following production steps by hot pressing (LaboPress P200 S, Vogt, 15 MPa, 130 °C, 5 min) and heat treatment (330 °C, 15 min, air atmosphere), burning out the methylcellulose and sintering the PTFE. This results in a mechanically stable electrode with a pore system that meets the requirements of a gas diffusion electrode. The electrode thickness and the catalyst load were determined using a thickness dial gauge (FD 50, Käfer) and weighing respectively. The properties of the ODC used in both experimental set-ups are shown in Table 1.

Experimental Set-Up with Electrolyte Convection

Electrochemical experiments were carried out in an in-house built half-cell with a flow-through electrolyte and gas chamber separated by the ODC. Measurements were recorded using a Gamry Reference 3000 potentiostat (Gamry Instruments, United Kingdom) with a three-electrode configuration. The ODC was operated as the working electrode, while a platinum wire was placed downstream in the electrolyte chamber as the counter electrode. Potentials were measured with respect to a reversible hydrogen electrode (RHE) (Hydroflex, Gaskatel, Germany) through a Luggin capillary ending in front of the working electrode. The electrolyte, 30 wt-% NaOH prepared from caustic flakes ($\geq$99 wt-%, Carl Roth, Germany) and demineralized water, was pumped through a heating tube and the half-cell from a heated reservoir providing a constant temperature of 50 °C. On the gas side pure oxygen was supplied with a flow rate of 50 $\mathrm{mL_N\ min^{-1}}$. The pressure on the electrolyte and gas side was set to 1.00×10^5 Pa. Sensors on the electrolyte and gas side monitored pressure and temperature. After a startup procedure ($-2\ \mathrm{kA\,m^{-2}}$ hold for 10 min, $-4\ \mathrm{kA\,m^{-2}}$ hold for 50 min, $-2\ \mathrm{kA\,m^{-2}}$ hold for 5 min), potential steps of 100 mV in the range from OCP (1.095 V vs. RHE) to 0.1 V vs. RHE were applied and the current response was recorded. After 30 s, current density values were extracted to record the polarization curve. For dynamic measurements the potential of 0.8 V vs. RHE was held for 30 s and stepped to 0.7 V vs. RHE. After a further 30 s, the step was reversed in the opposite direction.

Experimental Set-Up with SECM and Stagnant Electrolyte

For SECM the ODC was measured in an in-house built half-cell with a stagnant electrolyte above the electrode and the oxygen flow from below. The whole setup was built on an active damped table (Newport RS 2000, United States) to reduce noise. An in-house built faraday cage was equipped with isolating vacuumed polystyrene panels (Vaku-Isotherm, Germany) to ensure a constant temperature within the time scale of the experiments. The heat-conductive base plate was connected to a thermostat (Huber CC2, Germany) for the direct heating of the electrolyte to the operating temperature 50 °C. The oxygen back pressure ($\geq$99.5 %, Air Liquide, France) was regulated via a pressure controller (MKS Instruments, United States). All electronical components and the operator (using a foot connector; Conrad, Germany) were connected to the same ground, preventing ground loops and damages at the tip's apex.[23]

All electrochemical measurements were conducted utilizing an analogue bi-potentiostat (IPS PG 100, Germany) and the potentials were measured against a commercial RHE reference electrode (Mini Hydroflex, Gaskatel, Germany). A Pt mesh counter electrode was placed behind a thin D5 ceramic frit to prevent platinum species to diffuse to the working electrodes. All NaOH ($\geq$ 98.9 wt-%, J.T. Baker, The Netherlands) solutions were prepared with ultra-pure water (MilliQ, SG, Germany). In the measurements all solutions were air-saturated and heated up to 50 °C in a water bath to the required temperature before being filled into the pre-heated measurement cell. To ensure stable conditions at the sample electrode a conditioning procedure (cyclic voltammogramms, potential range between 0 to -1 V vs. RHE, 10 cycles, 100 $\mathrm{mV\,s^{-1}}$) was performed. After ODC conditioning the solution inside the cell was replaced to avoid an activity change of the electrolyte prior to the measurement. During the measurements the backside of the ODC was in contact with oxygen at 1.013×10^5 Pa, allowing passive oxygen transport. First the OCP of the ODC was determined as 1.1 V vs. RHE. Then the ODC was polarized step-wise between 1.1 V and 0.2 V vs. RHE. After the current at the initial potential reached the steady state, the potential was stepped 0.1 V in cathodic direction and the current was recorded for 100 s. From this measurement sequence the polarization and the current dependent NaOH activity were obtained. For dynamic analysis, an additional potential step from 0.8 V to 0.7 V and back to 0.8 V vs. RHE was recorded. Prior to the first step a steady state current was reached. The individual potential steps were recorded for 60 s.

SECM Electrode Fabrication and Measuring

As tip electrodes for the activity measurements platinum ultra micro electrodes (UME) were employed, which were prepared according to a previously published procedure.[24] Briefly, a laser puller (Sutter Instruments P-2000, United States) was utilized to pull Pt wires (Ø: 25 µm, Goodfellow, Germany) inside of quartz glass capillaries ($Ø_{out}$: 0.9 mm, $Ø_{in}$: 0.3 mm, L: 100 mm, QSIL, Germany) by sealing them in 10 to 12 cycles (20 s laser on and 40 s laser off) with the following parameters: Heat: 800, Filament: 5, Velocity: 128, Delay: 130, Pull: 0. Directly afterwards they were pulled: Heat: 820, Filament: 5, Velocity: 128, Delay: 130, Pull: 160. After soldering the Pt wire with soldering tin (Conrad, Germany) to a copper wire, the electrode tip was polished with an in-house built machine that rotates polishing paper and the electrode individually as described previously.[24] The electrochemical behavior as well as the active electrode size were subsequently determined in a solution of 5 mM $[\mathrm{Ru(NH_3)_6}]\mathrm{Cl_3}$ ($\geq$98 wt-%, Sigma Aldrich, Germany) in 100 mM KCl (100 wt-%, J.T. Baker, The Netherlands).

Pt UMEs were approached to the ODC by means of shear force distance-controlled scanning electrochemical microscopy (SECM). This technique is independent of the current signal and detects hydrodynamic forces in close proximity to the substrate surface.[25,26] Therefore, two piezo elements (Piezomechanik Pickelmann, Germany) were mounted to the electrode body at an angle of approx. 45°, ca. 1 to 1.5 cm distance from each other and individually connected to a lock-in amplifier (Ametek 7280, Germany). While the upper piezo oscillates the tip apex the lower one detects the resonance movement of the tip. Characteristic resonance frequencies were determined by comparison of frequency spectra (range: 200 to 500 kHz) in the bulk solution and within the shear force interaction distance (~200 nm above the surface). Pre-positioning of the tip at different lateral positions above the ODC surface was controlled using a video microscope (The ImagingSource USB-camera, Germany). A simplification of the previously reported 4D shear force-based constant-distance mode SECM[27] was used for precise positioning of the SECM tip, utilizing an analogue controlled piezo-based positioning system (PI, Germany). An automatic shear force-based approach curve was performed until a stop criterion of 5% of the lock-in magnitude value was reached. For all experiments, the tip (Ø: ~1 μm) was subsequently retracted to 1 μm to reach the final working distance for the cyclic voltammetry operation. The cyclic voltammetry was recorded at the platinum tip electrode (potential range was chosen according to the expected range between hydrogen and oxygen evolution potentials, $v = 0.05\ \mathrm{V\,s^{-1}}$) while the ODC was step-wise biased to a potential in between 0 and −1 V against its previously determined OCP. The activity of hydroxide and water was determined as described elsewhere.[8] In a short summary: By detection of cyclic voltammograms at a Pt nanoelectrode in the diffusion field above the ODC surface the Platinum oxide reduction peak was monitored. Considering that the potential of this reaction is dependent on the activity of hydroxide and water, the activity quotient of both species can be extracted applying the Nernst equation. Furthermore, a comparison to a previously recorded calibration curve in different concentrated NaOH solutions enables the direct evaluation of the NaOH concentration.

2. Modelling and Parameterization

2.1. Model

The one-dimensional three-phase thin-film model is divided into four spatially resolved sections, with three of them being located within the porous ODC (cf. Figure 2): A pure gas phase, a thin-film, which represents the interface of liquid and gas phase, and a porous electrode structure which is flooded by the liquid electrolyte, called flooded agglomerates. In addition, the fourth section is given by a liquid diffusion layer beyond the electrode. The equations of the validated model have been introduced in our previous work[6] and are shortly summarized in the following (cf. Table 2). Due to temperature-controlled experimental set-ups, isothermic behavior of the electrodes is assumed.

The Faradaic current density j_F is modeled by Farady's law eq. (2) and the Tafel equation (3). The overpotential of the ORR η_{reaction} is defined as the difference between the potential in the reaction zone E_{int} and the open circuit potential E_0 (cf. eq. (4)), where E_0 is calculated by the Nernst equation (5). Under further consideration of Ohm's law (cf. eq. (9)), and the double layer capacitance C_{dl}, the charge balance in the reaction zone is obtained (see eq. (10)). The mass transport across the porous electrode in the gas phase is described by the evaporation of water and the dissolution of oxygen at the gasliquid interface. The typically unequal absolute values of these two fluxes result in an overlaying convection, which is described by the bilateral non-equimolar diffusion eq. (11).[28] For calculating this convective Stefan flow, constant pressure p_{total} is assumed, which leads to the same velocity at every point in the gas phase (cf. eq. (14)). Thus, the velocity can be calculated from the fluxes of oxygen dissolution eq. (15) and water evaporation eq. (16). The specific surface of the gas-liquid interface is calculated by eq. (17). The mass transport in the thin-film is described by a diffusion process with an overlaying convection of all species due to evaporation. Since there are three species in the thin-film, Maxwell-Stefan diffusion eq. (18) has to be assumed. The convective flow is constant over the length of the thin-film, eq. (19), and calculated by eq. (20). The mass transport within the flooded agglomerates is also described by the Maxwell-Stefan diffusion with overlaying convection v_{liq}, but in a porous medium using eq. (21). Moreover, the change of the electrolyte density due to the ORR has to be modeled, which leads to an additional convection term between the reaction zone and the bulk phase eq. (22) and eq. (23). As shown in eq. (24), the local total velocity v_{liq} for each location z is calculated by the velocity of the evaporation $\upsilon_{\text{liq,evaporation}}$ and the location-dependent velocity due to the reaction $\upsilon_{\text{liq,react}}$. The mass transport in the liquid diffusion layer is described by the same equations as the mass transport within the flooded agglomerates, but with free diffusion (see eq. (25)); the convective velocity υ_{ldl} is equal to that at $z = z_{\text{l}}$ (cf. Figure 2) of the flooded agglomerates (cf. eq. (26) and eq. (27)). The boundary conditions are given in eq. (28)–(32). The model was implemented in Matlab.

2.2. Parameterization and Parameter Evaluation

Constant model parameters are adjusted to the operating conditions of the measurements and are listed in Table 3, concentration dependent parameters are given in Table 4. For the manual parameter identification, dynamic potential steps

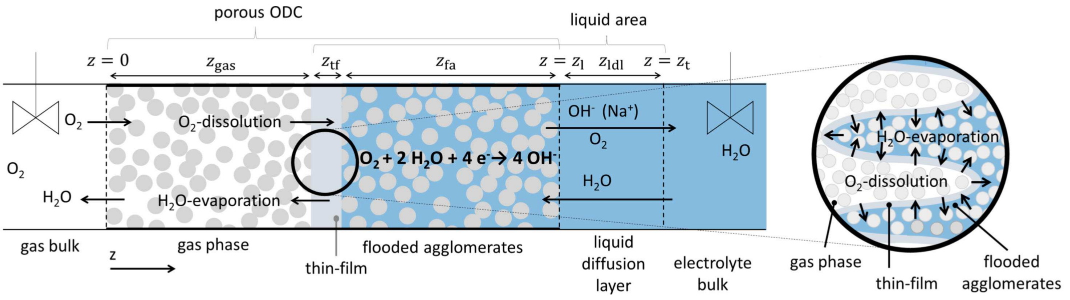

Figure 2. Schematic view of the model including reaction and mass transport. Right: Zoom at the gas-liquid interface.

Table 2. Model equations.

Electrochemical reaction kinetics, double layer capacitance and internal resistance		
Faraday current	$j_F = -\mathrm{F} \cdot 4 \cdot r$	(2)
Reaction rate	$r = k_0 \cdot a_{O_2} \cdot a_{H_2O}^2 \cdot exp\left(-\frac{(1-\alpha)\cdot \mathrm{F} \cdot \eta_{\mathrm{reaction}}}{\mathrm{R}\cdot T}\right)$	(3)
Reaction overpotential	$\eta_{\mathrm{reaction}} = E_{\mathrm{int}} - E_0$	(4)
Nernst equation	$E_0 = E_{00} + \frac{\mathrm{R}\cdot T}{4\cdot \mathrm{F}} ln\left(\frac{a_{O_2}\cdot a_{H_2O}^2}{a_{\mathrm{NaOH}}^4}\right)$	(5)
Activity of O_2	$a_{O_2} = x_{O_2} \cdot \gamma_{O_2}$	(6)
Activity of NaOH	$a_{\mathrm{NaOH}} = \frac{b_{\mathrm{NaOH}}}{b_{\mathrm{NaOH}}^{\Theta}} \cdot \gamma_{\pm}$	(7)
Molality of NaOH	$b_{\mathrm{NaOH}} = \frac{n_{\mathrm{NaOH}}}{m_{\mathrm{NaOH}}}$	(8)
Ohmic drop	$E_{\mathrm{ext}} - E_{\mathrm{int}} = R_{\mathrm{specific}} \cdot j$	(9)
Charge balance	$C_{\mathrm{dl}} \frac{\mathrm{d}E_{\mathrm{int}}}{\mathrm{d}t} = j - \mathrm{F} \cdot 4 \cdot r$	(10)
Mass transport in the gas phase and processes at the gas-liquid interface		
Species conservation	$\frac{\partial p_i}{\partial t} \cdot \varepsilon = -\frac{\partial^2 p_i}{\partial z^2} \cdot D_{i,j}^{\mathrm{gas,eff}} + \frac{\partial p_i}{\partial z} \cdot v_{\mathrm{gas}}$ with $i = \{H_2O, O_2\}$	(11)
Effective diffusion coefficient	$D_{i,j}^{\mathrm{gas,eff}} = D_{i,j}^{\mathrm{gas}} \cdot \frac{\varepsilon}{\tau}$	(12)
Bruggemann correlation	$\tau = \varepsilon^{-0.5}$	(13)
Local velocity	$\frac{\mathrm{d}\upsilon_{gas}}{\mathrm{d}z} = 0$	(14)
Henry's law	$c_{O_2}^* = \frac{p_{O_2}^*}{H_{O_2}(c_{\mathrm{NaOH}}^*, c_{H_2O}^*)}$	(15)
Stefan flow	$\frac{p_{\mathrm{total}}}{\mathrm{R}\cdot T} \cdot \upsilon_{\mathrm{gas}} = \dot{N}_{H_2O}^{\mathrm{evaporation}} - \dot{N}_{O_2}^{\mathrm{dissolution}}$	(16)
Specific surface area of interface	$S_{\mathrm{interface}} = \frac{A_{\mathrm{phase\ \ interface}}}{A_{\mathrm{geometric}}}$	(17)
Mass transport in the thin film		
Species conservation	$\frac{\partial c_i}{\partial t} = -\sum_{\substack{j=1\\ i\neq j}}^{n} \left(\frac{\partial^2 c_i}{\partial z^2}\frac{c_j}{c_{\mathrm{total}}} - \frac{\partial^2 c_j}{\partial z^2}\frac{c_i}{c_{\mathrm{total}}}\right) \cdot D_{i,j}^{\mathrm{liq}} + \frac{\partial c_i}{\partial z} \cdot \upsilon_{\mathrm{liq,evaporation}}$ with $i = \{OH^-, H_2O, O_2\}, j = \{OH^-, H_2O\}$	(18)
Local velocity (evaporation)	$\frac{\mathrm{d}v_{\mathrm{liq,evaporation}}}{\mathrm{d}z} = 0$	(19)
Velocity (evaporation)	$v_{\mathrm{liq,evaporation}} = \frac{\dot{N}_{H_2O}^{\mathrm{gas,in}}}{c_{H_2O}^*}$	(20)
Mass transport in the flooded agglomerates		
Species conservation	$\frac{\partial c_i}{\partial t} \cdot \varepsilon = -\sum_{\substack{j=1\\ i\neq j}}^{n} \left(\frac{\partial^2 c_i}{\partial z^2}\frac{c_j}{c_{\mathrm{total}}}\frac{\partial^2 c_j}{\partial z^2}\frac{c_i}{c_{\mathrm{total}}}\right) \cdot D_{i,j}^{\mathrm{liq,eff}} + \frac{\partial c_i}{\partial z} \cdot \upsilon_{\mathrm{liq}} - r$ with $i = \{OH^-, H_2O, O_2\}, j = \{OH^-, H_2O\}$	(21)
Velocity (reaction)	$v_{\mathrm{liq,react}}(z) = (\lvert\nu_{H_2O}^{\mathrm{ORR}}\rvert - \lvert\nu_{OH^-}^{\mathrm{ORR}}\rvert) \int_0^z \frac{r(z)}{c_{\mathrm{total}}} \mathrm{d}z$	(22)
Local velocity (reaction)	$\frac{\mathrm{d}v_{\mathrm{liq,react}}}{\mathrm{d}z} \neq 0$	(23)
Total velocity	$v_{\mathrm{liq}}(z) = v_{\mathrm{liq,evaporation}} + v_{\mathrm{liq,\ react}}(z)$	(24)
Mass transport in the liquid diffusion layer		
Species conservation	$\frac{\partial c_i}{\partial t} = -\sum_{\substack{j=1\\ i\neq j}}^{n} \left(\frac{\partial^2 c_i}{\partial z^2}\frac{c_j}{c_{\mathrm{total}}} - \frac{\partial^2 c_j}{\partial z^2}\frac{c_i}{c_{\mathrm{total}}}\right) \cdot D_{i,j}^{\mathrm{liq}} + \frac{\partial c_i}{\partial z} \cdot v_{\mathrm{ldl}}$ with $i = \{OH^-, H_2O, O_2\}, j = \{OH^-, H_2O\}$	(25)
Velocity	$v_{\mathrm{ldl}} = v_{\mathrm{liq}}(z = z_{\mathrm{l}})$	(26)
Local velocity	$\frac{\mathrm{d}v_{\mathrm{ldl}}}{\mathrm{d}z} = 0$	(27)
Boundary conditions		
O_2 in gas bulk	$p_{O_2}(z = 0) = p_{total}$	(28)
H_2O in gas bulk	$p_{H_2O}(z = 0) = 0$	(29)
O_2 in electrolyte bulk	$c_{O_2}(z = z_{\mathrm{t}}) = 0$	(30)
NaOH in electrolyte bulk	$c_{\mathrm{NaOH}}(z = z_{\mathrm{t}}) = c_{\mathrm{NaOH}}(z = z_{\mathrm{t}}, t = 0)$	(31)
H_2O in electrolyte bulk[a]	$c_{H_2O}(z = z_{\mathrm{t}}) = f(c_{\mathrm{NaOH}}(z = z_{\mathrm{t}}, t = 0))$	(32)
Electrode geometry	$z_{\mathrm{gas}} + z_{\mathrm{tf}} + z_{\mathrm{fa}} = z_{\mathrm{electrode}}$	(33)

[a] Calculated as in [15]

from 0.8 to 0.7 V vs. RHE and back to 0.8 V as well as an experimental polarization curve coupled with concentration measurements were used. The experimental data and simulation results will be discussed in the next section. The agreement between experiment and simulation is satisfactory for the polarization curves as well as the potential steps. The parameter values for both cells are presented in Table 5. The combination of stationary and dynamic measurements enables one to cover a wide operation range but also to determine the different processes in the electrode separately due to their characteristic time constants.

Table 3. List of constant parameters and operating conditions

Name	Symbol	Unit	Value	Source/ remarks
Electrode geometry				
Porosity	ε	–	0.4	[30]
Operating conditions				
Pressure in gas chamber	$P = P_{O_2}$	Pa	1.013×10^5	[a]
NaOH concentration in electrolyte bulk	$c_{NaOH}(z = z_t)$	$mol\,m^{-3}$	10.0×10^3	[a]
H_2O concentration in electrolyte bulk	$c_{H_2O}(z = z_t)$	$mol\,m^{-3}$	50.5×10^3	[15]
Temperature	T	K	323.15	[a]
Electrochemical and kinetic data				
Charge transfer coefficient	α_{ORR}	–	0.15	[31][b]
Stoichiometric coefficient H_2O	$\nu_{H_2O}^{ORR}$	–	-2	
Stoichiometric coefficient OH^-	$\nu_{OH^-}^{ORR}$	–	$+4$	
Binary diffusion coefficients				
For gaseous oxygen/water	D_{O_2,H_2O}^{gas}	$m^2\,s^{-1}$	2.48×10^{-5}	[32]
For liquid oxygen/water	D_{O_2,H_2O}^{liq}	$m^2\,s^{-1}$	1.36×10^{-9}	[32, 33][c]
For liquid oxygen/NaOH	$D_{O_2,NaOH}^{liq}$	$m^2\,s^{-1}$	2.02×10^{-9}	[32, 33][c]
For liquid water/ NaOH	$D_{H_2O,NaOH}^{liq}$	$m^2\,s^{-1}$	5.33×10^{-10}	[34][d]

[a] Experimental operating condition; [b] Measured with 6.5 M NaOH; [c] Calculated with modified Wilke and Chang equation, with $\Theta = 3.9$ and $a = 0{,}5$ chosen adjusted to experimental data from [33]; [d] No NaOH data available, modeled for KOH with NaOH viscosity from [35].

Table 4. Electrolyte concentration dependent variables.

Name	Symbol	Unit	Source/remarks
Inverse Henry constant	H_{O_2}	$Pa\,m^3\,mol^{-1}$	[36][a]
Activity coefficient of O_2	γ_{O_2}	–	[13]
Activity of H_2O	a_{H_2O}	–	[11]
Mean activity coefficient of NaOH	$\gamma_\pm$	dimensionless¹	[37]
Density of electrolyte	ρ	$kg\,m^{-3}$	[35]
Water vapor pressure	$p_{H_2O}^{vap}$	Pa	[15]

[a] Extrapolated from $c_{\mathrm{NaOH}} \leq 6M$, but as shown in [9] extrapolated values fit very well to experiments with $c_{\mathrm{NaOH}} \leq 12M$.

Table 5. Parameters identified from electrochemical experiments.

Name	Symbol	Unit	Convective electrolyte	Stagnant electrolyte
Reaction rate constant	k_0	$mol\,s^{-1}\,m^{-2}$	15.42×10^4	9.20×10^4
Specific interface	$S_{interface}$	$m^2\,m^{-2}$	56.0	36.4
Liquid diffusion layer thickness	z_{ldl}	m	10×10^{-6}	270×10^{-6}
Overall specific resistance	$R_{specific}$	$\Omega\,m^2$	1.16×10^{-4}	1.82×10^{-4}
Length of flooded agglomerates	z_{fa}	m	7.90×10^{-6}	8.14×10^{-6}
Thin-film thickness[a]	z_{tf}	m	80×10^{-9}	
Double layer capacitance	C_{dl}	$F\,m^{-2}$	80	720

[a] Set as equal for both systems.
Typical values for the thin-film thicknesses: 25–300 nm.[38]

As expected, significantly different values for both systems are obtained for the length of the liquid boundary layer z_{ldl} in and the electrolyte bulk phase: $z_{ldl}^{con} = 10\ \mu m$ for the set up with the convective electrolyte flow and $z_{ldl}^{stag} = 270\ \mu m$ for the set-up with the stagnant electrolyte. For the reaction rate constant k_0, the specific interface $S_{interface}$ and the average length of flooded agglomerates z_{fa}, both systems exhibits values in the same order of magnitude. The larger specific interface in the cell with the convective electrolyte flow may occur due to the higher motion in the liquid electrolyte and is associated with temporary local shifts of the gas-liquid interface on the pore scale level. The large differences in double layer capacitances may be explained by its dependency on the current densities,[29] which differs considerably in both systems at the respective potentials. Additional possible measurement inaccuracies are discussed below.

In our previous work dealing with ODC operated at 80 °C, we presented a higher value of $S_{interface} = 134\ m^2\,m^{-2}$ and a slightly higher value for z_{fa} of 11.5 µm.[6] On the one hand this deviation may originate from temperature dependent system characteristics like viscosity or wettability. On the other hand, the use of dynamic measurements in our present work allows for a better separation and a more precise identification of the process parameters.

3. Steady State Analysis of ODC Performance

Figure 3 displays the measured and the simulated polarization curves of both systems. In the kinetically governed regime at small current densities both cells have almost the same behavior, which is expected, since similar electrodes were used. Accordingly, the derived reaction rate constants k_0 (cf. Table 5) are in the same order of magnitude.

In contrast, at medium current densities up to the diffusion limited current density, a strong difference between both systems occurs: While the system with the stagnant electrolyte

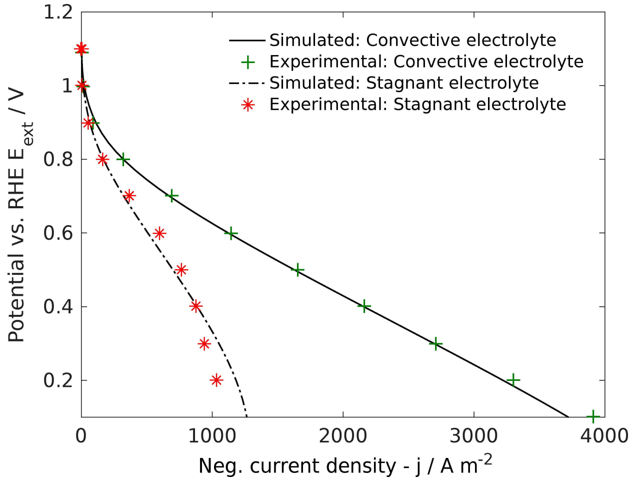

Figure 3. Simulated polarization curves in comparison to experimental polarization curves for convective electrolyte flow and stagnant electrolyte cell.

shows a significant mass transport limitation at about $j \approx 1.3\ \mathrm{kA\,m^{-2}}$ at $E_{\mathrm{Ext}} = 0.1$ V vs. RHE, no mass transport limitation proceed for the system with electrolyte convection at $j = 3.8\ \mathrm{kA\,m^{-2}}$ at the same potential.

The ORR can proceed at locations within the flooded agglomerates where the reactants oxygen and water both are present. In the following, this section is called reaction zone. In Figure 4, simulated oxygen concentration profiles over the thin-film and the first micrometer of the flooded agglomerates for both systems at different current densities are shown. For both systems the reaction zone, facing the gas-liquid interface, decreases in size with increasing current densities due to the depletion of oxygen. Similarly to what is presented in our previous work,[6] no oxygen associated limitation takes place due to the mass transport in the gas phase, therefore all oxygen mass transport limitation can be attributed to the liquid phase. In the system with the stagnant electrolyte, the reaction zone shrinks to almost zero at the mass transport governed current density of $j \approx 1.3\ \mathrm{kA\,m^{-2}}$. This shows that the limiting current density is determined by the availability of the oxygen. In contrast, for the system with the convective electrolyte flow, the reaction zone amounts to several nanometers even at a current density of $j = 3.8\ \mathrm{kA\,m^{-2}}$ so that no oxygen mass transport limitation occurs. The vast disparity in oxygen availability is caused by the difference of current dependent water activity inside the electrodes. The ORR consumes water and produces hydroxide ions within the reaction zone close to the gas-liquid interface. Since three to four water molecules form a solvation shell around the hydroxide ion,[12] the amount of free water molecules and thus the water activity decreases significantly due to the production of hydroxide ions. This change of water activity leads to a change of the phase equilibrium of water and oxygen, and thus to a reduced oxygen solubility[13] and a higher vapor pressure of water.[15] There is also experimental evidence for the accumulation of hydroxide ions in the system with the stagnant electrolyte: Figure 5 shows the hydroxide ion concentrations detected via SECM 1 µm above the ODC surface (cf. Figure 1), in comparison to the simulated values at the same location. It can be deduced that both, the measurement as well as the model, show a significant increase of hydroxide concentration and subsequently a decrease of the water activity. Differences between experiment and simulation amounts to max 10% and might result from additional convection caused by a temperature gradient or local inhomogeneities of ion concentration in-plane direction of the electrode in the experiment.[8] The mass transport resistance for the exchange of water and hydroxide ions between the ODC and the electrolyte bulk is much higher for the thick liquid diffusion layer in the system with the stagnant electrolyte than in the system with the convective electrolyte flow. A thicker diffusion layer constitutes a larger diffusion resistance and causes a higher accumulation of hydroxide ions in the electrode. Thus, the accumulation of the hydroxide has a detrimental effect on the oxygen solubility, which is higher in

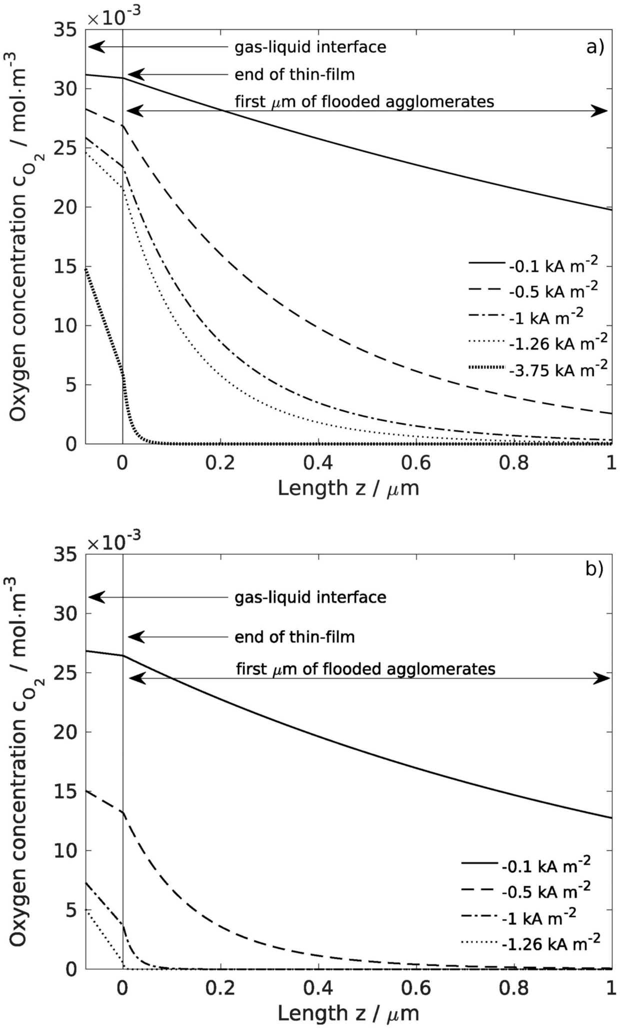

Figure 4. Dependence of simulated oxygen concentrations profiles within the liquid phase with respect to the current density for a) convective electrolyte flow, b) stagnant electrolyte.

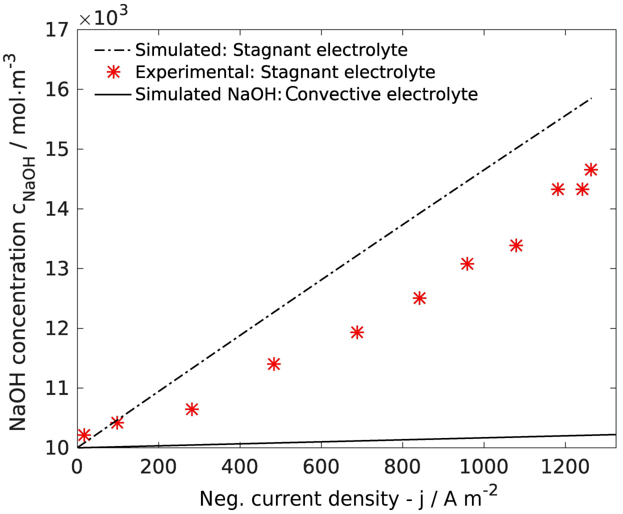

Figure 5. Simulated and experimental NaOH concentration in the liquid diffusion layer 1 µm above the ODC surface for cell with stagnant electrolyte. For comparison, NaOH concentration in the cell with the convective electrolyte flow is also given at the same location.

the system with the stagnant electrolyte than in the system with the convective electrolyte flow.

This in turn explains why the system with the stagnant electrolyte is limited by oxygen availability at $E = 0.1$ V vs. RHE.

4. Dynamic Analysis

In this section the influence of the reaction-induced oxygen solubility limitation on the dynamics of the ODC is discussed in detail based on dynamic measurements and simulations of both configurations. In Figure 6, the current response to a potential step from 0.8 to 0.7 V vs. RHE and back is displayed for both systems. Although the same potential is applied to both electrodes, the system with electrolyte convection offers a higher cathodic current density, which agrees with the polarization curves and has been discussed in the previous section. Furthermore, both systems exhibit a very different dynamic response to the potential step, which will be discussed individually. Two distinct processes can be separated: The charging and discharging of the double layer and the mass transport of water and hydroxide ions across the liquid phase. As discussed below, the dynamics of the oxygen follow the latter process.

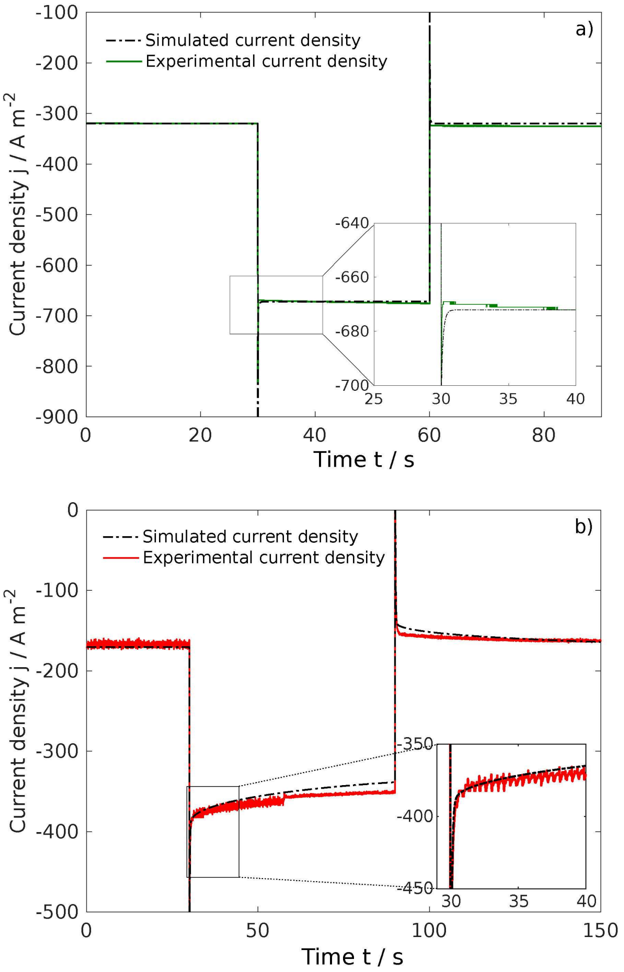

Figure 6. Simulated and experimental time-dependent current density response for a potential step from 0.8 to 0.7 V vs. RHE at $t = 30$ s and a) back at $t = 60$ s for convective electrolyte flow cell, b) back at $t = 90$ s for stagnant electrolyte cell.

The charging and discharging of the double layer is the reason for the positive and negative current peaks directly after the positive and the negative potential step. For both systems, different time constants are obtained, which is attributed to the dependency of the double layer capacitance on the current density.[29] Additional a lager area outside the reactive area due to small leakages between the sealing ring and the ODC of the double layer may be penetrated in the smaller cell with the stagnant electrolyte. Since the electrode circumference/area ratio is approx. 3.5 times larger for the smaller cell than for the lager cell with the convective electrolyte flow, this effect may be more significant.

The subsequent relaxation of the current density occurring in the range of seconds is dominated by the mass transport of water and hydroxide ions between the reaction zone and the electrolyte bulk phase.[6] The corresponding time constant can be approximated with equation (34), derived from Fick's second law:

$$\tau_{\mathrm{mt}} \approx \frac{\Delta z^2}{D} \tag{34}$$

With τ_{mt} as the time constant of water and hydroxide ion mass transport, D as the diffusion coefficient and Δz as the mass transport length. For both systems the mass transport time constant is a function of the diffusion through the porous structure of the flooded agglomerates and the free diffusion through the liquid diffusion layer (cf. Figure 2), which can be calculated separately. Since the length of the flooded part of both electrodes is almost the same, similar time constants are obtained: $\tau^{\mathrm{fa,con}}_{\mathrm{mt,H_2O}} = 0.46$ s for the convective electrolyte flow and $\tau^{\mathrm{fa,stag}}_{\mathrm{mt,H_2O}} = 0.49$ s for the stagnant electrolyte. In contrast, the time constants for the mass transport across the liquid diffusion layer differs by orders of magnitude between both systems: $\tau^{\mathrm{ldl,con}}_{\mathrm{mt,H_2O}} = 0.19$ s and $\tau^{\mathrm{ldl,stag}}_{\mathrm{mt,H_2O}} = 181.3$ s. The large time constant is in line with the observation that no steady state is reached within the 60 s duration of the dynamic test for the system with the stagnant electrolyte, but within 1 s for the system with the convective electrolyte flow. In conclusion, the water and hydroxide ion transport across the liquid diffusion layer dominates the current response to the potential step and causes the large difference in the current response of both electrodes. The corresponding time dependent ion concentration and water activity at the gas-liquid interface and 1 µm away from the ODC surface are presented in Figure 7. Due to the relationship between water and hydroxide activity as discussed above, the two activities show opposite trends. Furthermore, water activity has a strong influence on oxygen solubility.[11] This effect is illustrated in Figure 8 for the system with the stagnant electrolyte. The right-hand side of the plot displays the steady state water activity gradient within the liquid diffusion layer for $t = 30$ s directly before the negative potential step and at selected time points afterwards. The plot in the middle shows the same process within the flooded

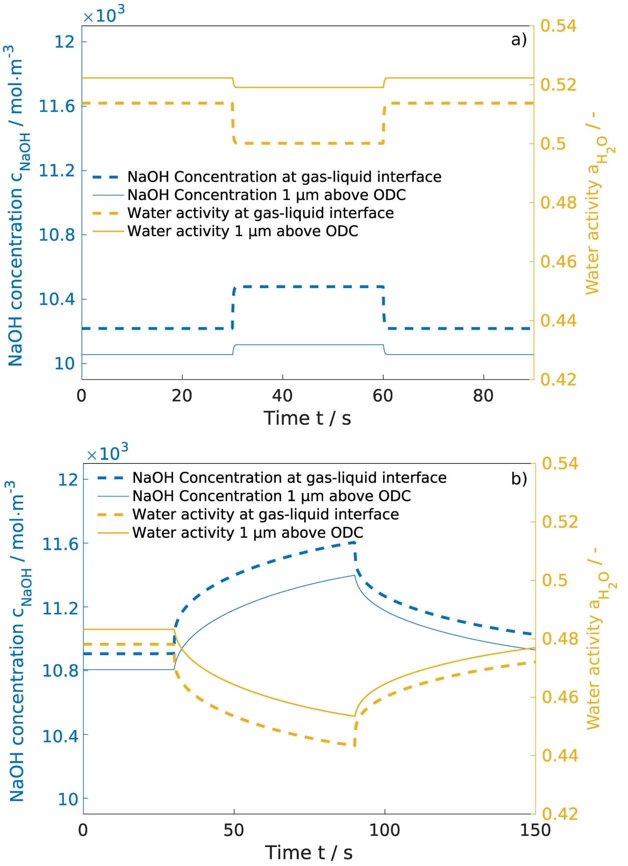

Figure 7. Simulated NaOH concentration and water activity within the liquid phase dependent on the time for a potential step from 0.8 to 0.7 V vs. RHE at $t=30$ s and a) back at $t=60$ s for convective electrolyte flow cell, b) back at $t=90$ s for stagnant electrolyte cell.

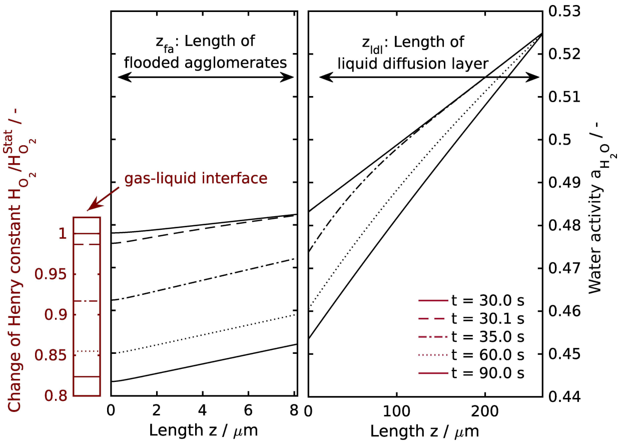

Figure 8. Henry constant at the gas-liquid interface (left) at steady state current at 0.7 V vs. RHE and its change at selected time points after a potential step to 0.8 V vs. RHE. Corresponding gradient of water activity within the ODC across the flooded agglomerates (middle) and in the liquid diffusion layer (right). Cell with no electrolyte convection.

agglomerates. A comparison of the curves suggests that the gradient over the whole electrode and the liquid diffusion layer change with a delay. This is due to the fast reaction rate compared to slow mass transport of water and hydroxide ions.

The plot on the left-hand side of Figure 8 depicts the corresponding change of oxygen solubility for the different points in time, indicated by the relative change of the Henry constant at the gas-liquid interface during the step. The change of the Henry constant directly affects the oxygen solubility. In the cell with electrolyte convection the liquid diffusion layer is smaller and the new steady state of the phase equilibrium and thus of oxygen concentration is reached much faster.

The resulting response of oxygen concentration with and without electrolyte convection is depicted in Figure 9 for different locations. It can be inferred that due to the ion dependent solubility the oxygen concentration is governed by the same time constant as the ion concentration. Therefore, the oxygen supplied to the reaction zone and thus the current density exhibits the same time constants as the liquid phase mass transfer.

In Figure 6, deviations between experiments and simulations are visible, which are discussed in the following. For the system with electrolyte convection, a slight decrease of the negative current density with time after the negative potential

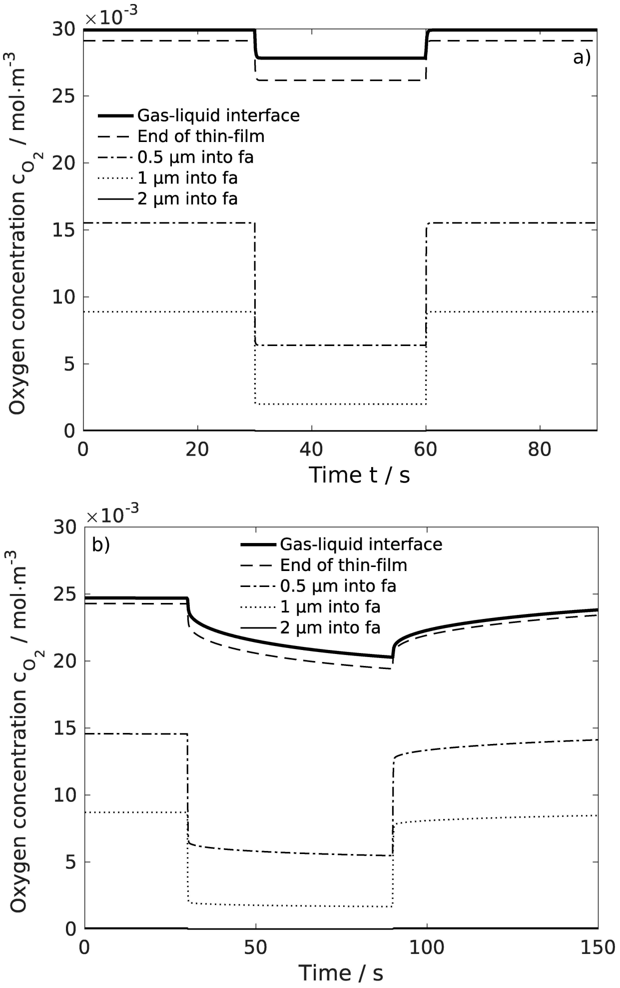

Figure 9. Simulated oxygen concentration within the liquid phase dependent on the time for a potential step from 0.8 to 0.7 V vs. RHE at $t=30$ s and a) back at $t=60$ s for convective electrolyte flow cell, b) back at $t=90$ s for stagnant electrolyte cell. (fa: flooded agglomerates).

step at 30 s can be identified in the experiment. For the system without electrolyte convection, the measured current density is more cathodic than the simulated one. Different factors which are not included in the model might have contributed to this behavior: Although the experiments were conducted under temperature control, a moderate increase of the ODC temperature which would improve kinetics and transport processes, cannot be excluded. In that regard, heating effects can be caused by ohmic losses or the entropy effect, for instance.[39] Also conceivable is the influence of the micro kinetics considering hydrogen peroxide formation and catalyst loading with hydrogen ions,[40] which are not considered by the assumed lumped kinetics. The same effects may occur for the steady state results shown above.

From the dynamic analysis, we can conclude that the performance as well as the dynamics of the ODC is determined by the mass transport across the liquid phase. This insight is corroborated by two main aspects: On the one hand, in the system with the stagnant electrolyte, water activity decreases only by less than 7.5% as a consequence of the negative potential step, but oxygen solubility decreases by 18% (cf. Figure 8). This suggests a minor influence of the water activity on the kinetics in a direct way but a high indirect impact due to the oxygen solubility. On the other hand, due to the faster water mass transport, the oxygen solubility of the system with the convective electrolyte flow only decreases by 7%. The comparison of both systems indicates that the mass transport within the liquid electrolyte has a significant influence on the electrode performance. It is expected that also electrode design and temperature will have significant impact, as they are known to affect transport phenomena. This leads to the conclusion that the performance of technical ODC can be improved by accelerating the mass transfer in the liquid phase, e.g. via convective electrolyte flow or electrolyte flow field optimization. Already now, in industrial application quite high performances are reached due to convective electrolyte transport in so called percolators,[41] further performance increase might be reached by a even further optimized mass transport.

5. Conclusions

Experimental polarization curves and potential steps demonstrate that the performance and dynamic behavior of ODC deviate strongly when the electrodes are operated with and without convection of the liquid electrolyte. Without electrolyte convection, a mass transfer limitation is reached at a current density of $j \approx 1.3\ \mathrm{kA\,m^{-2}}$, whereas this does not occur at current densities of $j > 3.9\ \mathrm{kA\,m^{-2}}$ with electrolyte convection. Furthermore, the dynamic response of the current density to a potential step exhibits a significantly slower relaxation behavior without electrolyte convection.

By comparing both systems utilizing simulation and measurements, the hypothesis that water activity plays a key role was confirmed. The accumulation of hydroxide ions leads to a reduction in water activity and thus in oxygen solubility. Since three to four water molecules are bound to every hydroxide ion as a solvation shell, the water activity decreases rapidly as a function of the ionic strength, and the accompanying change of the phase equilibrium leads to a lower oxygen solubility. The model-based analysis suggests that electrolyte convection increases mass transfer rates in the liquid phase which in turn reduces the hydroxide ion accumulation and thereby increases both, water activity and oxygen solubility. Without electrolyte convection, a thicker liquid diffusion layer is established causing a stronger accumulation of hydroxide ions and a lower water activity. Not all processes can be explained by mass transport and phase equilibrium phenomena, so that further research on catalyst activity and micro kinetics within porous structures is needed.

In conclusion, a high mass transport rate of water and hydroxide ions is essential for high ODC performance and needs to be ensured for technical applications of these kind of electrodes. A thorough understanding of the transport processes is also indispensable for understanding the dynamic behavior of the electrodes.

List of Symbols

A	Area ($\mathrm{m^2}$)
a_i	Activity of species i (–)
b_i	Molality of species i ($\mathrm{mo\,kg^{-1}}$)
C_{dl}	Double layer capacitance ($\mathrm{F\,m^{-2}}$)
c_i	Concentration of species i ($\mathrm{mol\,m^{-3}}$)
D_{ij}	Binary diffusion coefficient for species i and j ($\mathrm{m^2\,s^{-1}}$)
E	Potential (V)
E_0	Open circuit potential (V)
E_{00}	Standard electrode potential (V)
F	Faraday constant (=96485.34) ($\mathrm{C\,mol^{-1}}$)
H	(Inverse) Henry constant ($\mathrm{Pa\,m^3\,mol^{-1}}$)
j	Current density ($\mathrm{A\,m^{-2}}$)
k_0	Reaction rate constant ($\mathrm{mol\,s^{-1}\,m^{-2}}$)
$\dot{N}_i$	Mass flow density of species i ($\mathrm{mol\,s^{-1}\,m^{-2}}$)
p	Pressure (Pa)
p_i	Partial pressure of species i (Pa)
R	Universal gas constant (=8.3145) ($\mathrm{J\,mol^{-1}\,K^{-1}}$)
R_{specific}	Specific resistance ($\Omega\,\mathrm{m^2}$)
r	Reaction rate ($\mathrm{mol\,s^{-1}}$)
$S_{\mathrm{interface}}$	Specific surface area of the interface (–)
T	Temperature (K)
t	Time (s)
v	Velocity ($\mathrm{m\,s^{-1}}$)
x_i	Mole fraction of species i (–)
z	Length (m)
α	Charge transfer coefficient (–)
ε	Porosity (–)
γ_i	Activity coefficient of species i (–)
$\gamma_{\pm}$	Mean activity coefficient of NaOH (–)
η_{reaction}	Reaction overpotential (V)
Θ	Loading ($\mathrm{mg\,cm^{-2}}$)
ν_i^{ORR}	Stoichiometric coefficient of species i in ORR (–)
τ	Tortuosity (–)

Sub- and superscripts

con	Convective electrolyte flow
eff	Effective
ext	External
F	Faradaic
fa	Flooded agglomerates
gas	Gaseous/gas phase
int	Internal
l	Liquid/liquid phase
ldl	Liquid diffusion layer
stag	Stagnant electrolyte
t	Total
tf	Thin-film
Θ	Standard state

Acknowledgement

The authors are thankful to the Deutsche Forschungsgemeinschaft (DFG) for funding this research in the framework of the Forschungsgruppe "Multi-scale analysis of complex three-phase systems: oxygen reduction on gas-diffusion electrodes in aqueous electrolyte" (FOR 2397; research grants TU 89/13-1, SCHU 929/15-1 and KR 3850/6-1).

Conflict of Interest

The authors declare no conflict of interest.

Keywords: Oxygen reduction reaction · Scanning electrochemical microscopy · Local ion activity · Gas diffusion electrodes · Mass transfer effects

[1] F. Kubannek, T. Turek, U. Krewer, *Chem. Ing. Tech.* **2019**, *91*, 720–733.
[2] R. Kuwertz, I. G. Martinez, T. Vidaković-Koch, K. Sundmacher, T. Turek, U. Kunz, *Electrochem. Commun.* **2013**, *34*, 320–322.
[3] I. Moussallem, J. Jörissen, U. Kunz, S. Pinnow, T. Turek, *J. Appl. Electrochem.* **2008**, *38*, 1177–1194.
[4] M. Chatenet, L. Genies-Bultel, M. Aurousseau, R. Durand, F. Andolfatto, *J. Appl. Electrochem.* **2002**, *32*, 1131–1140.
[5] D. Franzen, B. Ellendorff, M. C. Paulisch, A. Hilger, M. Osenberg, I. Manke, T. Turek, *J. Appl. Electrochem.* **2019**, *49*, 705–713.
[6] M. Röhe, F. Kubannek, U. Krewer, *ChemSusChem* **2019**, *11*, 2373–2385.
[7] J. Clausmeyer, A. Botz, D. Öhl, W. Schuhmann, *Faraday Discuss.* **2016**, *193*, 241–250.
[8] A. Botz, J. Clausmeyer, D. Öhl, T. Tarnev, D. Franzen, T. Turek, W. Schuhmann, *Angew. Chem. Int. Ed.* **2018**, *57*, 12285–12289.
[9] C. Zhang, F. R. F. Fan, A. J. Bard, *J. Am. Chem. Soc.* **2009**, *131*, 177–181.
[10] M. J. Blandamer, J. B. F. N. Engberts, P. T. Gleeson, J. C. R. Reis, *Chem. Soc. Rev.* **2005**, *34*, 440–458.
[11] G. Åkerlöf, G. Kegeles, *J. Am. Chem. Soc.* **1940**, *62*, 620–640.
[12] A. Botti, F. Bruni, S. Imberti, M. A. Ricci, A. K. Soper, *J. Chem. Phys.* **2004**, *120*, 10154–10162.
[13] S. L. Clegg, P. Brimblecombe, *Geochim. Cosmochim. Acta* **1990**, *54*, 3315–3328.
[14] A. Botti, F. Bruni, S. Imberti, M. A. Ricci, A. K. Soper, *J. Chem. Phys.* **2003**, *119*, 5001–5004.
[15] H. G. Hirschberg, *Handbuch Verfahrenstechnik und Anlagenbau*. Springer-Verlag Berlin Heidelberg New York, **1999**.
[16] Q. Mao, U. Krewer, *Electrochim. Acta* **2013**, *103*, 188–198.
[17] U. Krewer, M. Christov, T. Vidaković, *J. Electroanal. Chem.* **2006**, *589*, 148–159.
[18] D. Schröder, V. Laue, U. Krewer, *Comput. Chem. Eng.* **2016**, *84*, 217–225.
[19] U. Krewer, F. Röder, E. Harinath, R. D. Braatz, B. Bedürftig, R. Findeisen, *J. Electrochem. Soc.* **2018**, *165*, A3656–A3673.
[20] Q. Mao, U. Krewer, *Electrochim. Acta* **2012**, *68*, 60–68.
[21] D. Öhl, D. Franzen, M. Paulisch, S. Dieckhöfer, S. Barwe, C. Andronescu, I. Manke, T. Turek, W. Schuhmann, *ChemSusChem* **2019**, *12*, 2732–2739.
[22] I. Moussallem, S. Pinnow, N. Wagner, T. Turek, *Chem. Eng. Process.* **2012**, *52*, 125–131.
[23] N. Nioradze, R. Chen, J. Kim, M. Shen, P. Santhosh, S. Amemiya, *Anal. Chem.* **2013**, *85*, 6198–6202,.
[24] B. Ballesteros Katemann, W. Schuhmann, *Electroanalysis* **2002**, *14*, 22–28.
[25] R. Brunner, A. Bietsch, O. Hollricher, O. Marti, *Rev. Sci. Instrum.* **1997**, *68*, 1769–1772.
[26] M. Ludwig, C. Kranz, W. Schuhmann, H. E. Gaub, *Rev. Sci. Instrum.* **1995**, *66*, 2857–2860.
[27] M. Nebel, K. Eckhard, T. Erichsen, A. Schulte, W. Schuhmann, *Anal. Chem.* **2010**, *82*, 7842–7848.
[28] B. Kögl, *Grundlagen der Verfahrenstechnik*. Springer Vienna, Vienna, **1981**.
[29] G. D. Polcyn. Charakterisierung und Modellierung der Sauerstoffreduktion an Sauerstoff-Verzehr-Kathoden für die Chlor-Alkali-Elektrolyse anhand von Abschaltmessungen, 2018. Technische Universität Dortmund, *Dissertation*.
[30] S. Pinnow, N. Chavan, T. Turek, *J. Appl. Electrochem.* **2011**, *41*, 1053–1064.
[31] Prosper, K. Adanuvor, *J. Electrochem. Soc.* **1988**, *135*, 2509.
[32] B. E. Poling, J. M. Prausnitz, J. P. O'Connell, *The Properties of Gases and Liquids*. McGraw Hill professional. McGraw-Hill Education, **2000**.
[33] M. Chatenet, M. Aurousseau, R. Durand, *Ind. Eng. Chem. Res.* **2000**, *39*, 3083–3089.
[34] J. Newman, D. Bennion, C. W. Tobias, *Ber. Bunsen-Ges.* **1965**, *69*, 608–612.
[35] J. Oisson, I. A. Jernqvist, G. I. Aly, *Int. J. Thermophys.* **1997**, *18*.
[36] D. Tromans, *Ind. Eng. Chem. Res.* **2000**, *39*, 805–812.
[37] J. Balej, *Collect. Czech. Chem. Commun.* **1996**, *61*, 1549–1562,.
[38] F. G. Will, D. J. Bendaniel, *J. Electrochem. Soc.* **1969**, *116*, 933–937.
[39] N. Chavan, S. Pinnow, G. D. Polcyn, T. Turek, *J. Appl. Electrochem.* **2015**, *45*, 899–912.
[40] A. Ignaczak, R. Nazmutdinov, A. Goduljan, L. M. de Campos Pinto, F. Juarez, P. Quaino, E. Santos, W. Schmickler, *Nano Energy* **2016**, *29*, 362–368.
[41] J. Kintrup, M. Millaruelo, V. Trieu, A. Bulan, Ernesto S. Mojica, *Electrochem. Soc. Interface* **2017**, *26*, 73–76.

Manuscript received: July 23, 2019
Revised manuscript received: September 27, 2019
Accepted manuscript online: September 27, 2019